J. Fluid Mech. (2016), *vol.* 788, *pp.* 576–601.
doi:10.1017/jfm.2015.679

Lattice Boltzmann simulations of low-Reynolds-number flow past fluidized spheres: effect of Stokes number on drag force

Gregory J. Rubinstein[1], **J. J. Derksen**[2] **and Sankaran Sundaresan**[1,†]

[1]Department of Chemical and Biological Engineering, Princeton University, Princeton, NJ 08540, USA

[2]Department of Chemical Engineering, Delft University of Technology, 2628 BL Delft, Netherlands

(Received 14 July 2015; revised 7 October 2015; accepted 12 November 2015)

In a fluidized bed, the drag force acts to oppose the downward force of gravity on a particle, and thus provides the main mechanism for fluidization. Drag models that are employed in large-scale simulations of fluidized beds are typically based on either fixed-particle beds or the sedimentation of particles in liquids. In low-Reynolds-number (*Re*) systems, these two types of fluidized beds represent the limits of high Stokes number (*St*) and low *St*, respectively. In this work, the fluid–particle drag behaviour of these two regimes is bridged by investigating the effect of *St* on the drag force in low-*Re* systems. This study is conducted using fully resolved lattice Boltzmann simulations of a system composed of fluid and monodisperse spherical particles. In these simulations, the particles are free to translate and rotate based on the effects of the surrounding fluid. Through this work, three distinct regimes in the characteristics of the fluid–particle drag force are observed: low, intermediate and high *St*. It is found that, in the low-*Re* regime, a decrease in *St* results in a reduction in the fluid–particle drag. Based on the simulation results, a new drag relation is proposed, which is, unlike previous models, dependent on *St*.

Key words: fluidized beds, particle/fluid flow, suspensions

1. Introduction

Constitutive models for the fluid–particle drag force are widely utilized in the analysis of fluidized suspensions of solid particles (Sundaresan 2000). In fluidized beds, the buoyant weight of particles is principally balanced by the drag force exerted by the flowing fluid. As a result, the quantitative accuracy of model predictions depends critically on the accuracy of drag force models. Therefore, in order to achieve quantitative precision in the study of fluidized beds, such as those used in the pharmaceuticals or oil industries, it is vital to accurately model the drag force at the particle-scale level. Despite this fact, there are a number of limitations to the drag models that are currently available in the literature, one of which is the inability to account for the effect of particle translation and rotation. This particular limitation is addressed and remedied through the current work.

† Email address for correspondence: sundar@princeton.edu

Models for the fluid–particle drag force have arisen through analytical (Brinkman 1947; Kim & Russel 1985; Koch & Sangani 1999), experimental (Darcy 1856; Kozeny 1927; Carman 1937; Ergun 1952; Richardson & Zaki 1954; Wen & Yu 1966; Garside & Al-Dibouni 1977; Davis & Acrivos 1985; Gidaspow 1994; Nguyen & Ladd 2005) and computational methods (Hill, Koch & Ladd 2001; van der Hoef, Beetstra & Kuipers 2005; Beetstra, van der Hoef & Kuipers 2007; Tenneti, Garg & Subramaniam 2011). These drag relations seek to account for the interactions between fluid and particles over a range of particle volume fraction, ϕ, and Reynolds number, Re. For a fluid–particle system, the particle volume fraction, ϕ, is defined as

$$\phi = \frac{NV_p}{V_{tot}}, \tag{1.1}$$

where V_p is the particle volume, and N is the number of particles in the system of interest with volume V_{tot}, while the Reynolds number is defined as

$$Re = \frac{\rho_f(1-\phi)|\boldsymbol{u}_s|d_p}{\mu_f}, \tag{1.2}$$

where ρ_f is the fluid density, μ_f is the dynamic fluid viscosity, d_p is diameter of the particle and $\boldsymbol{u}_s$ is the slip velocity, which is the difference between the fluid velocity, $\boldsymbol{u}_f$, and the particle velocity, $\boldsymbol{v}_p$. Constitutive relations for the fluid–particle drag force are often cast in terms of a dimensionless drag force, F, which is defined as

$$F = \frac{\boldsymbol{f}_{fp} \cdot \boldsymbol{u}_s}{\boldsymbol{F}_{d,Stokes} \cdot \boldsymbol{u}_s}, \tag{1.3}$$

where $\boldsymbol{f}_{fp}$ is the total fluid–particle interaction force minus the generalized buoyancy arising from the slowly varying stress field, and the Stokes drag relation on a single spherical particle at infinite dilution in a viscous fluid is given by

$$\boldsymbol{F}_{d,Stokes} = 3\pi\mu_f d_p \boldsymbol{u}_s. \tag{1.4}$$

Thus, the quantity F can be thought of as a quantitative measure of the deviation from the ideal Stokes behaviour ($\phi \to 0$ and $Re \to 0$).

In the literature, two of the more commonly employed fluid–particle drag relations are the models of Wen & Yu (1966) and Beetstra *et al.* (2007). In drag studies like that of Beetstra *et al.* (2007), highly resolved numerical simulations based on the lattice Boltzmann method (LBM) are used to study the flow of fluid past a fixed bed of solid particles. On the other hand, drag relations, like that of Wen & Yu (1966), are developed from sedimentation experiments. At the low-Re limit, the drag relation of Beetstra *et al.* (2007) as a function of ϕ is given by the model of van der Hoef *et al.* (2005):

$$F_{van\,der\,Hoef}(\phi) = \frac{10\phi}{1-\phi} + (1-\phi)^3(1+1.5\sqrt{\phi}), \tag{1.5}$$

while the equation of Wen & Yu (1966) is given by

$$F_{Wen\text{–}Yu} = (1-\phi)^{-(n-2)}, \tag{1.6}$$

with $n = 4.65$ (Wen & Yu 1966). In figure 1, the dimensionless drag curves of Wen & Yu (1966) and van der Hoef *et al.* (2005) as functions of ϕ are compared. Key

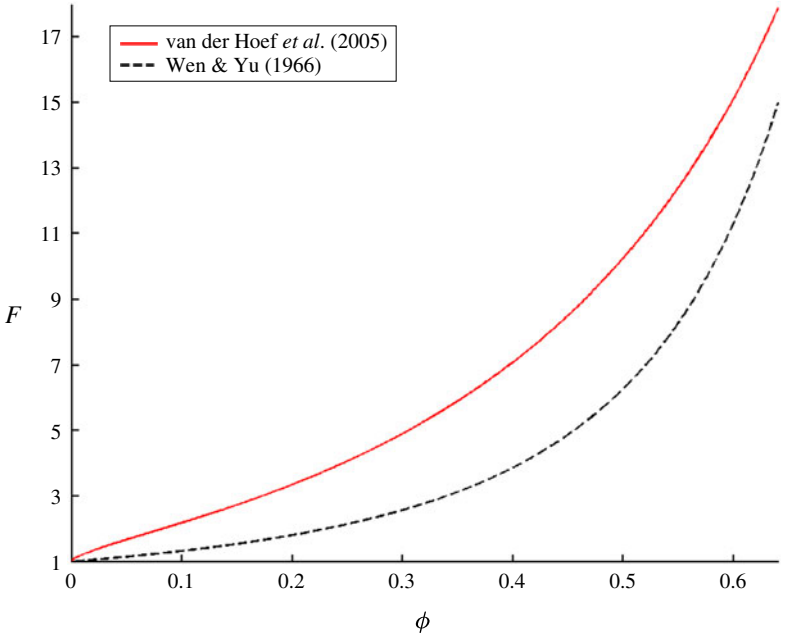

FIGURE 1. (Colour online) The dimensionless drag force, F, as a function of the particle volume fraction, ϕ, is plotted for both the model of van der Hoef *et al.* (2005) (low-*Re* limit of the model of Beetstra *et al.* (2007)) and that of Wen & Yu (1966) at the low-*Re* limit. From this figure, it is clear that $F_{van\,der\,Hoef} > F_{Wen\text{–}Yu}$ over the entire range of ϕ.

similarities between these two drag curves are that $F \to 1$ as $\phi \to 0$, and F increases monotonically as ϕ increases. In the low-*Re* regime, the dimensionless drag of van der Hoef *et al.* (2005) is significantly greater than the drag of Wen & Yu (1966) over the entire range of ϕ. The critical distinction between these two types of fluid–particle systems is that in the case of van der Hoef *et al.* (2005), the particles are fixed in place and therefore unable to rotate and translate, while in the case of Wen & Yu (1966), the rotational and translational velocities of the particles are able to quickly adapt to the effects of the surrounding flow, which allows the fluid to move through with less drag. The Stokes number, *St*, which is defined as

$$St = \frac{\rho_p(1-\phi)|\boldsymbol{u}_s|d_p}{18\mu_f} = \frac{\rho_p}{\rho_f}\frac{Re}{18}, \tag{1.7}$$

where ρ_p is the particle density, can be used to characterize this distinction. Here *St* is the ratio of the particle relaxation time to the fluid relaxation time, and so it is a critical parameter for quantifying the resistance of the particles to changes in their translational and rotational velocities due to the surrounding fluid flow. From this definition, the fixed bed (in the case of van der Hoef *et al.* (2005)) represents the high-*St* limit of fluidized systems, while the sedimentation of solid particles in liquid (in the case of Wen & Yu (1966)) represents the low-*St* limit behaviour.

Even though the drag models of Wen & Yu (1966) and Beetstra *et al.* (2007) are derived from starkly different flow conditions and have significantly different values (figure 1), they are often applied interchangeably. In the work of Igci & Sundaresan (2011) and Ozel, Fede & Simonin (2013), the model of Wen & Yu (1966) is used

as the drag closure for the large-scale simulations of a gas–solid fluidized bed, while in similar studies, Pepiot & Desjardins (2012) and Radl & Sundaresan (2014) instead employ the model of Beetstra *et al.* (2007). Thus, there is a great deal of ambiguity in the fluidization literature about the applicability of the different drag models, particularly in terms of the different *St* limits. Li & Kuipers (2003) found that the predicted flow behaviour of a fluidized bed can be very sensitive to the form of the fluid–particle drag force, and so achieving precision in large-scale modelling of fluidized beds relies heavily on using drag relations that are truly applicable to the system of interest.

The current work looks to determine a drag model that is applicable to low-*Re* fluidized systems over a full range of *St* and ϕ. Towards this goal, LBM simulations are employed, in which, unlike the majority of prior LBM drag studies, the particles are allowed to freely translate and rotate based on the effects of the surrounding fluid. In doing so, the effects of particle translation and rotation are accounted for in a drag relation that bridges the transition from the low-*St* regime (Wen & Yu (1966) type model) to the high-*St* regime (van der Hoef *et al.* (2005) or Beetstra *et al.* (2007) model). Due to the fact that the drag model derived from the current work is valid over the entire range of *St* and ϕ, its application to larger-scale simulation studies of fluidized beds will result in greater quantitative precision.

In § 2, we summarize the simulation method. In § 3, we present the simulation results and provide the equation for the drag model that accounts for both *St* and ϕ in the low-*Re* regime. Finally, in § 4, we provide some concluding remarks on the overall findings of this work.

2. Simulation method

2.1. *Numerical set-up for the LBM scheme*

In LBM, the fluid flow is simulated by the movement of fluid parcels along a three-dimensional lattice of nodes (Benzi, Succi & Vergassola 1992). The movement from one node to its neighbour is governed by the Boltzmann equation, which is discretized in both time and space. It can be demonstrated that the equations that describe the fluid dynamics obey the incompressible Navier–Stokes equations in the low-Mach-number limit (Chen & Doolen 1998; Aidun & Clausen 2010). LBM, which dates back to the work of McNamara & Zanetti (1988), was first employed in the study of fluid flows in the works of Higuera & Jimenez (1989), Higuera & Succi (1989) and Higuera, Succi & Benzi (1989). The scheme used in this study for the evolution of the fluid density and momentum distributions is described by Somers (1993) and Eggels & Somers (1995). This implementation is a slight variant of the widely used LBGK scheme (Qian, d'Humieres & Lallemand 1992), with a more stable behaviour at low viscosities and second-order accuracy in space and time. LBM was first used to study the interaction between fluid and solid particles by Ladd (1994). In the current scheme, the no-slip condition at the boundaries between the fluid and particles is handled with a forcing scheme, which is similar to the immersed boundary method (Goldstein, Handler & Sirovich 1993; Derksen & van den Akker 1999; ten Cate *et al.* 2002). This type of method for resolving the fluid–particle boundary, which utilizes an internal fluid, is stable for values of ρ_p/ρ_f that are sufficiently larger than one (ten Cate *et al.* 2002). In this forcing scheme, additional forces are imposed on the fluid at the surface of the solid sphere, such that the fluid velocity matches the local velocity of the solid surface. The force and torque that the fluid exerts on a solid particle are then computed by summing over these local forces that are needed to maintain a no-slip condition at the particle's surface.

There are a number of subgrid particle–particle interaction forces that are explicitly included in the LBM scheme. As two particles approach each other, the accuracy of the LBM breaks down due to a lack of spatial resolution in the gap between the particles (Ladd 1997). An additional particle–particle lubrication force is therefore introduced in order to account for the contributions of the unresolved part of the flow field (Kim & Karilla 1991; Nguyen & Ladd 2002). Further details of the numerical scheme used in our study can be found in the work of Derksen & Sundaresan (2007).

In order to facilitate the computational scheme for modelling the particle–particle collisions, the particles are assigned a degree of softness. This softness is characterized by a collision time, t_c, between two particles. The Hookean spring constant, k, for the elastic collisions is defined as

$$k = \frac{\pi^3 \rho_p d_p^3}{6 t_c^2}. \tag{2.1}$$

A particle–particle interaction force therefore arises due to these soft collisions. In this work, the collision between particles is assumed to be elastic and frictionless. For all of the simulations in the current study, t_c is taken to be 10 LBM time steps, which corresponds to a maximum particle–particle overlap of about $0.001 d_p$. The total force and torque acting on each particle are then used in the equations of motion to update each particle's velocity and position.

Spherical monodisperse particles are used in the current LBM simulations. The input diameter, in units of lattice spacing, is specified for the particles. Because the spherical particle is defined over a cubic grid, the effective hydrodynamic diameter of the spherical particle, d_p, differs slightly from the input diameter. A calibration procedure, based on the work of Ladd (1994), is used to determine d_p from the input diameter and kinematic viscosity, ν_f, of the fluid. Larger values of d_p correspond to a more fully resolved fluid flow profile and thus a finer grid resolution.

Throughout the current study, fully periodic boundary conditions in all three dimensions are employed. Furthermore, a body force is applied to both the particles and fluid in order to drive flow in the system, as described by Derksen & Sundaresan (2007). This body force can be interpreted as the superposition of a downward gravity force and an upward pressure gradient. In this periodic system, the strength of the pressure gradient is set such that the total body force on the fluid and particles is zero. Since $\rho_p > \rho_f$, the net body force on the particles is downward, while the net body force on the fluid is upward. Since the lattice units are dimensionless, the lattice spacing, Δ, and the time step are simply taken to be 1. For a given simulation system, the key parameters that need to be provided are d_p, ν_f, the particle-to-fluid density ratio, ρ_p/ρ_f, the strength of the applied external body force, f_{ext}, the total number of particles, N, and the dimensions of the lattice, n_x, n_y and n_z. Additionally, the initial coordinates of each of the particles are provided. From (1.1), the domain-averaged particle volume fraction, $\overline{\phi}$, is determined from N, d_p and the system dimensions. For a typical simulation in the current study, d_p is taken to be 12, ν_f is taken to be 0.1 and n_x, n_y and n_z are all taken to be $6 d_p$. A study of the sensitivity of the observed fluid–particle dynamics to changes in the grid resolution is provided in § 3.2.2. Furthermore, f_{ext} and ρ_p/ρ_f are both varied over a range of values, such that the flow remains in the low-Re regime but a large range of St is sampled. It is important to note that because Re and St are both functions of $\boldsymbol{u}_s$, they are not set *a priori*. Instead, these parameters are determined from the results of the simulations.

In this study, we also investigated the characteristics of systems at the two limits of St: a high-St limit bed (fixed bed) and a low-St limit bed. The additional constraints

that must be applied to simulations of high-*St* and low-*St* limit beds are discussed in the following section.

2.2. *Simulating high- and low-St limit cases*

In order to gain a more complete understanding of the behaviour of fluidized beds at the two *St* limits, high and low, we look to simulate these two cases using the LBM scheme. However, in order to simulate the proper dynamics of these two limiting cases, additional constraints are necessary. These constraints are ascertained by analysing the effect of *Re* and *St* on the governing equations of motion.

The equation of motion for the position of a single particle is given as

$$\frac{\mathrm{d}\boldsymbol{x}_p}{\mathrm{d}t} = \boldsymbol{v}_p, \tag{2.2}$$

where $\boldsymbol{x}_p$ is the position of the particle. In a fluidized suspension, the linear momentum balance for a spherical particle is given by

$$\rho_p \frac{\pi}{6} d_p^3 \frac{\mathrm{d}\boldsymbol{v}_p}{\mathrm{d}t} = (\rho_p - \overline{\rho})\frac{\pi}{6} d_p^3 \boldsymbol{g} + \boldsymbol{f}_{fp}, \tag{2.3}$$

where $\overline{\rho} = \overline{\phi}\rho_p + (1-\overline{\phi})\rho_f$ is the mixture density and $\boldsymbol{g}$ is the gravitational acceleration vector. Other forces, like particle–particle contact, which are included in the LBM simulations, can be added to the right-hand side of (2.3), but for the purposes of simplifying the current analysis, they are not included. Furthermore, the angular momentum balance for the spherical particle is given by

$$\rho_p \frac{\pi}{60} d_p^5 \frac{\mathrm{d}\boldsymbol{\Omega}_p}{\mathrm{d}t} = \boldsymbol{T}, \tag{2.4}$$

where $\boldsymbol{\Omega}_p$ is the angular velocity of the particle and $\boldsymbol{T}$ is the torque of the fluid acting on the particle.

The equations of motion for the fluid phase are given as

$$\frac{\partial(\rho_f(1-\phi))}{\partial t} + \nabla\cdot(\rho_f(1-\phi)\boldsymbol{u}_f) = \boldsymbol{0}, \tag{2.5}$$

$$\frac{\mathrm{D}_f}{\mathrm{D}t}(\rho_f(1-\phi)\boldsymbol{u}_f) = -(1-\phi)\nabla p' + (1-\phi)(\rho_f - \overline{\rho})\boldsymbol{g} - (1-\phi)\nabla\cdot\boldsymbol{\tau}_f - \frac{6}{\pi}\frac{\phi}{d_p^3}\boldsymbol{f}_{fp}, \tag{2.6}$$

where $\boldsymbol{\tau}_f$ is the deviatoric fluid stress tensor and $\mathrm{D}_f/\mathrm{D}t$ is the total fluid material derivative with respect to time. $\nabla p'$ is the rapidly varying pressure gradient term, where the total pressure gradient, ∇p, is given by $\nabla p = \overline{\rho}\boldsymbol{g} + \nabla p'$. At the surface of each particle, no-slip and no-penetration boundary conditions are imposed.

Using a scaling analysis, in which we look to retain all of the contributions to the net force (right-hand side in (2.3) and (2.6)) and assume that ρ_f does not vary, we obtain the following set of non-dimensional governing equations:

$$\frac{\mathrm{d}\tilde{\boldsymbol{x}}_p}{\mathrm{d}\tilde{t}} = \tilde{\boldsymbol{v}}_p, \tag{2.7}$$

$$St_c \frac{\mathrm{d}\tilde{\boldsymbol{v}}_p}{\mathrm{d}\tilde{t}} = \tilde{\boldsymbol{g}} + \tilde{\boldsymbol{f}}_{fp}, \tag{2.8}$$

$$St_c \frac{\mathrm{d}\tilde{\boldsymbol{\Omega}}_p}{\mathrm{d}\tilde{t}} = \widetilde{\boldsymbol{T}}. \tag{2.9}$$

$$\frac{\partial(1-\phi)}{\partial\tilde{t}} + \tilde{\boldsymbol{\nabla}} \cdot ((1-\phi)\tilde{\boldsymbol{u}}_f) = \boldsymbol{0}, \tag{2.10}$$

$$Re_c \frac{\mathrm{D}_f}{\mathrm{D}\tilde{t}}((1-\phi)\tilde{\boldsymbol{u}}_f) = -(1-\phi)\tilde{\boldsymbol{\nabla}}\tilde{p}' - 18\left(\frac{\overline{\rho}-\rho_f}{\rho_p-\overline{\rho}}\right)(1-\phi)\tilde{\boldsymbol{g}} - (1-\phi)\tilde{\boldsymbol{\nabla}}\cdot\tilde{\boldsymbol{\tau}}_f - 18\phi\tilde{\boldsymbol{f}}_{fp}, \tag{2.11}$$

where $\tilde{\boldsymbol{x}}_p = \boldsymbol{x}_p/d_p$, $\tilde{\boldsymbol{v}}_p = \boldsymbol{v}_p/u_c$, $\tilde{t} = t/(d_p/u_c)$, $\tilde{\boldsymbol{g}} = \boldsymbol{g}/g$, $\tilde{\boldsymbol{f}}_{fp} = \boldsymbol{f}_{fp}/(3\pi d_p\mu_f u_c)$, $\tilde{\boldsymbol{\Omega}}_p = \boldsymbol{\Omega}_p/(u_c/d_p)$, $\widetilde{\boldsymbol{T}} = \boldsymbol{T}/(3\pi d_p^2\mu_f u_c/10)$, $\tilde{\boldsymbol{\nabla}} = d_p\boldsymbol{\nabla}$, $\tilde{\boldsymbol{u}}_f = \boldsymbol{u}_f/u_c$, $\tilde{p}' = p'/(\mu_f u_c/d_p)$ and $\tilde{\boldsymbol{\tau}}_f = \boldsymbol{\tau}_f/(\mu_f u_c/d_p)$. In these expressions, the characteristic superficial slip velocity is $u_c = (1-\phi_c)|\boldsymbol{u}_{s,c}|$, where the subscript c denotes a characteristic quantity, and $g = |\boldsymbol{g}|$. Furthermore, the characteristic Stokes number, St_c, and characteristic Reynolds number, Re_c, are given by

$$St_c = \frac{\rho_p u_c d_p}{18\mu_f}, \tag{2.12}$$

$$Re_c = \frac{\rho_f u_c d_p}{\mu_f}. \tag{2.13}$$

It is clear that (2.12) and (2.13) have the same form as (1.7) and (1.2), respectively. Furthermore, u_c is chosen such that the drag force balances the force of gravity and the effects of the imposed pressure gradient on a single particle at infinite dilution:

$$u_c = \frac{(\rho_p - \overline{\rho})d_p^2 g}{18\mu_f}. \tag{2.14}$$

From this non-dimensionalization, the effect of St and Re on the equations governing particles and fluid can be ascertained.

Focusing on the left-hand side of (2.7)–(2.11), it is observed that Re multiplies the term $(\mathrm{D}_f/\mathrm{D}\tilde{t})((1-\phi)\tilde{\boldsymbol{u}}_f)$, St multiplies the terms $\mathrm{d}\tilde{\boldsymbol{v}}_p/\mathrm{d}\tilde{t}$ and $\mathrm{d}\tilde{\boldsymbol{\Omega}}_p/\mathrm{d}\tilde{t}$, and the term $\mathrm{d}\tilde{\boldsymbol{x}}_p/\mathrm{d}\tilde{t}$ is multiplied by 1. The high- and low-St limit cases are then cast in terms of these dimensionless groups: Re, St and 1. Since the current study focuses on the low-Re regime, $Re \ll 1$. Thus, in the high-St limit, $Re \ll 1 \ll St$, and so the particle velocities (both linear and angular) evolve over a much longer time than do the particle positions, which, in turn, evolve over a much longer time than does the fluid velocity. Thus, the fluid velocity field is in a quasisteady state (QSS) relative to the particle positions and velocities. In the low-St limit, Re, $St \ll 1$, and so the particle positions evolve over a much longer time than do the particle velocities and fluid velocity. The fluid and particle velocities, therefore, are in a QSS relative to the particle positions.

It is important to specify that Re refers to the Reynolds number based on the mean slip velocity. We can express $\boldsymbol{v}_p$ and $\boldsymbol{\Omega}_p$ as

$$\boldsymbol{v}_p = \langle \boldsymbol{v}_p \rangle + \boldsymbol{v}_p', \tag{2.15}$$

$$\boldsymbol{\Omega}_p = \langle \boldsymbol{\Omega}_p \rangle + \boldsymbol{\Omega}_p', \tag{2.16}$$

where $\langle \boldsymbol{v}_p \rangle$ and $\langle \boldsymbol{\Omega}_p \rangle$ are the average linear and angular velocities, respectively, of all of the particles in the simulation region. We use $\boldsymbol{v}_p'$ and $\boldsymbol{\Omega}_p'$ to denote the

corresponding fluctuations from the mean value. Since $\langle \boldsymbol{\Omega}_p \rangle = \mathbf{0}$ in our systems of interest, we can consider two additional Reynolds numbers based on the two fluctuation velocities:

$$Re_T = \frac{\rho_f d_p}{\mu_f} \sqrt{\frac{1}{3} \langle \boldsymbol{v}_p' \cdot \boldsymbol{v}_p' \rangle}, \tag{2.17}$$

$$Re_\Omega = \frac{\rho_f d_p^2}{\mu_f} \sqrt{\frac{1}{3} \langle \boldsymbol{\Omega}_p' \cdot \boldsymbol{\Omega}_p' \rangle}, \tag{2.18}$$

where the notation $\langle\,\rangle$ is used to designate a quantity that is averaged over all of the particles in the system. In this study, we limit our attention to $Re_T, Re_\Omega, Re \ll 1$. In gas–solid systems of moderate to high Re, Wylie, Koch & Ladd (2003) and Kriebitzsch, van Der Hoef & Kuipers (2013) demonstrated the significance of the effect of fluctuations in the velocities of the particles, quantified by the granular temperature, on the fluid–particle drag force. However, in low-Re systems, these effects of granular temperature are found to be less pronounced. Furthermore, recent work by Zhou & Fan (2014) has used LBM simulations to look at additional contributions to the fluid–particle interaction force besides the drag force, namely the Magnus lift force, which arises due to the effects of strong particle rotation. However, in the current study, the flow conditions are such that the drag force is the single dominant contribution to the overall interaction force. In these systems, the fluid–particle interaction forces that are perpendicular to the slip velocity, like the Magnus lift force, represent less than 1 % of the total interaction force.

2.2.1. *High-St limit*

At the high-St limit ($Re \ll 1 \ll St$), the fluid relaxes very quickly compared with the particles, and so the fluid is in a QSS relative to the particles. In the reference frame where $\langle \boldsymbol{v}_p \rangle = \mathbf{0}$, the high-$St$ fluidized system is characterized by a mean fluid velocity, $\langle \boldsymbol{u}_f \rangle$, $\boldsymbol{v}_p'$ and $\boldsymbol{\Omega}_p'$. Since $Re_T, Re_\Omega, Re \ll 1$, this system can be interpreted as a linear superposition of the following three systems: (1) a fixed-bed system, in which there is a mean fluid velocity, $\langle \boldsymbol{u}_f \rangle$, but $\boldsymbol{v}_p' = \boldsymbol{\Omega}_p' = \mathbf{0}$; (2) a system in which the particles have fluctuations in their linear velocities, but $\langle \boldsymbol{u}_f \rangle = \boldsymbol{\Omega}_p' = \mathbf{0}$; and (3) a system in which the particles have fluctuations in their angular velocities, but $\langle \boldsymbol{u}_f \rangle = \boldsymbol{v}_p' = \mathbf{0}$. Since there is no mean flow in systems (2) and (3), these systems do not contribute to the overall fluid–particle drag force. Thus, the drag force for the overall high-St fluidized system arises solely from system (1). Thus, the high-St limit case can be represented by a fixed-particle bed. In the LBM simulations of the high-St limit case, the fluid moves around the fixed particles, and eventually a QSS flow distribution is established for a given particle configuration and external driving force. Since the particles do not translate or rotate in any way to adjust to the surrounding flow, the high-St limit provides the upper limit for the dimensionless drag force, F, in the low-Re regime.

2.2.2. *Low-St limit*

At the low-St limit (Re, $St \ll 1$), the fluid and particle velocities are in a QSS relative to the particle positions. In this case, the velocities (linear and angular) of the particles evolve much faster than their positions, as the particles respond immediately to the flow. Lattice Boltzmann simulations, in which the particle positions are frozen, are used as a computational method for finding the QSS velocities of the particles and fluid. At each step in the simulations, the particle velocities are updated, as usual, based on the net forces and torques acting on each particle. The particle positions, on the other hand, are not changed. As these simulations converge to a steady state, the net force and torque on each particle approach zero. The computed equilibrium

velocity profile provides the dynamics for a low-*St* limit bed at a single instant in time. Since the linear and angular velocities of the particles adjust very quickly to the flow of the surrounding fluid, the low-*St* limit provides the lower limit for F in a low-*Re* fluidized bed.

3. Simulation results

3.1. *High-St limit with a random array of particles*

The high-*St* limiting behaviour is established by simulating a fixed-particle bed, as motivated in § 2.2.1. It is understood that all of the relevant Reynolds numbers are small, leaving *St* and ϕ as the only dimensionless quantities of interest for the present study. For each simulation, the particles are arranged in a random, homogeneous configuration. To obtain each random configuration, the particles are thermalized using a discrete element method (DEM) simulation. This thermalization method places particles in the DEM simulation box at random, assigning each particle a random velocity from a Gaussian distribution. The particles are then allowed to move around and collide without the effects of the fluid or gravity. After each particle has undergone many collisions, a snapshot of the DEM simulation is taken. The random, homogeneous configuration of particles for the LBM simulations is then obtained from this DEM snapshot. In this case and throughout the study, the dimensionless drag force, F (1.3), is computed by averaging the fluid velocity, particle velocities and fluid–particle interaction forces over the entire domain (Euler–Euler approach). In these domain-averaged calculations, the values of ϕ and $\overline{\phi}$ are equivalent. The data that are used to compute F for a fixed bed are taken from a snapshot of the system after the steady state has been reached. A particle diameter of $d_p = 12$ and a kinematic fluid viscosity of $\nu_f = 0.1$ are used for these simulations. These fixed-bed simulations are conducted over a wide range of ϕ values. For each value of ϕ, the results are averaged over a large number (between 10 and 60) of random, homogeneous particle configurations. Since the particle positions are held fixed and all of the simulations are conducted in the low-*Re* regime, the high-*St* drag results are independent of f_{ext} and ρ_p/ρ_f. In figure 2, the results for F as a function of ϕ are presented for three different cubic periodic domain sizes: $n_x = 6d_p$, $9d_p$ and $12d_p$. From figure 2, we see that the effect of the domain size on the high-*St* limit case is negligible. Furthermore, from figure 2, we see that the high-*St* limit drag curve matches very closely the drag curve (1.5) of van der Hoef *et al.* (2005), which was also computed for fixed-particle systems. This result confirms the validity of the current LBM numerical scheme. This same set of parameters, with a cubic domain size of $n_x = 6d_p$ and a grid resolution of $d_p = 12$ and $\nu_f = 0.1$, is used for the majority of the current study.

3.2. *Simulations of fluidized beds*

Relaxing the constraint that the particles have to be held fixed in place, we then look to study the dynamics of a fluidized bed, in which the particles are free to translate and rotate based on the forces and torques that act on them. For each fluidized bed simulation, f_{ext} and ρ_p/ρ_f are specified. The initial configuration of particles is random and homogeneous, and is obtained using a DEM thermalization technique. As time evolves, the particle positions change as particle structures and voids form in the system. The data that are used to compute F for a fluidized bed are taken from snapshots of the system after a statistical steady state has been reached. At each of these snapshots in time, taken from simulations of fluidized beds, we extract the particle positions, fluid and particle velocities, as well as the fluid–particle interaction forces. The criterion for determining the statistical steady state is based on the time

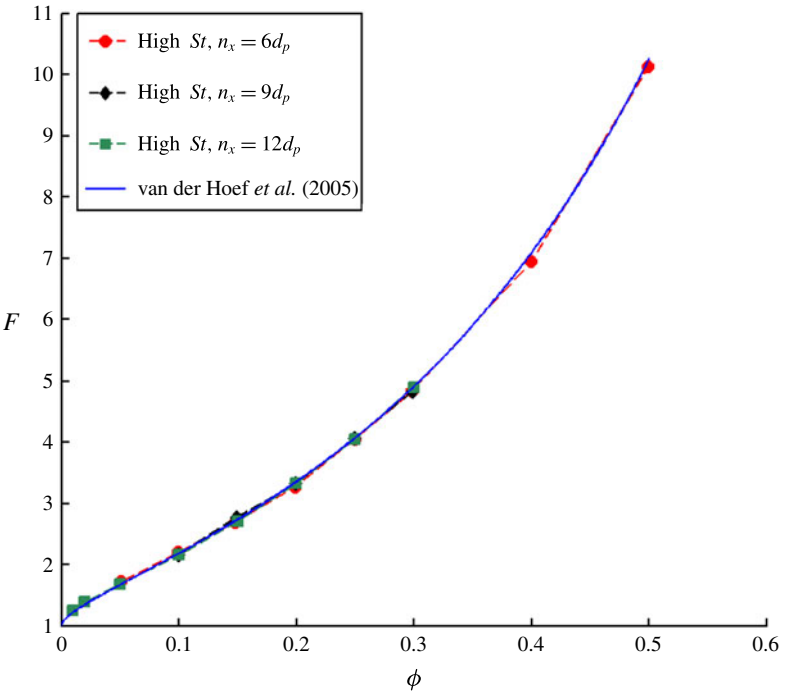

FIGURE 2. (Colour online) The dimensionless drag force, F, is computed over a range of domain-averaged particle volume fractions, ϕ, for a fixed-particle bed (high-St limit), for three different cubic periodic domain sizes: $n_x = 6d_p$, $9d_p$ and $12d_p$. The effects of the domain size appear to be negligible for the high-St limit case. These drag curves match very closely the drag curve of van der Hoef *et al.* (2005).

evolution of the domain-averaged slip velocity (as shown in the inset to figure 3). Due to the mobility of the particles, the slip velocity does not approach a single steady-state value, as in the fixed-bed simulations, so the statistical steady state is based on the time-averaged slip velocity approaching a constant value. As in the high-St limit case, an Euler–Euler averaging approach is used for determining the values of F. For each set of ρ_p/ρ_f, f_{ext} and ϕ, the value of F is determined by averaging over the results of 10 different initial particle configurations. Since St is a function of the slip velocity, it is determined, like F, by averaging over the results of the different initial particle configurations.

3.2.1. *Effect of domain size on the dynamics of fluidized beds*

In figure 3, the results for F over a range of ϕ for a $St = 11.5$ fluidized bed are presented for three different cubic periodic domain sizes: $n_x = 6d_p$, $9d_p$ and $12d_p$. The value of f_{ext} is set such that Re is of the order of 0.1, and properly adjusted in order to achieve the desired value of St, which we show in § 3.6 is the key parameter for the current study. From figure 3, over the entire range of ϕ, there is a significant decrease in F as the domain size, n_x, increases. Due to the mobility of particles in the fluidized case, as the domain size increases, the length scale over which particle structures form increases, which leads to an increase in the extent of flow-induced inhomogeneities in the distribution of particles. Increases in the extent of inhomogeneities lead to the formation of larger voids in the system. The fluid is

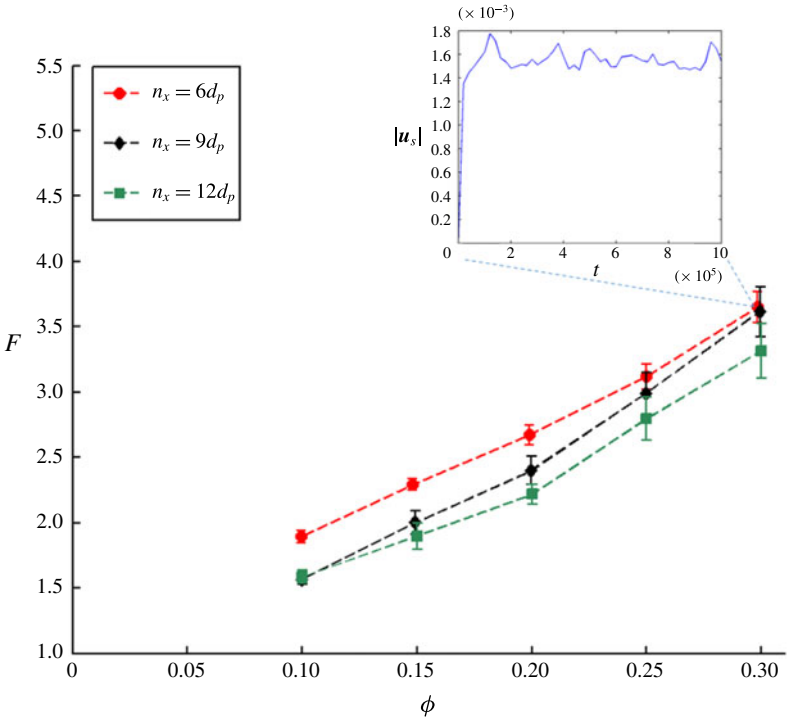

FIGURE 3. (Colour online) F is computed over a range of domain-averaged particle volume fractions, ϕ, for a $St = 11.5$ fluidized bed for three different cubic periodic domain sizes: $n_x = 6d_p$, $9d_p$ and $12d_p$. For all of these cases, $d_p = 12$ and $\nu_f = 0.1$. As n_x increases, there is a decrease in the value of F. This drag reduction is due to an increase in the extent of inhomogeneities in the particle configuration that comes from increases in the domain size. In the inset to this figure, the magnitude of the fluid–particle slip velocity, $|\boldsymbol{u}_s|$, is plotted as a function of time for the case of $\phi = 0.3$, $n_x = 6d_p$. This type of plot is used to determine when the fluidized bed has reached a statistical steady state.

able to preferentially move through these larger voids, leading to a smaller overall fluid–particle drag force, thus explaining the reduction in F as n_x increases. While there is a clear effect of domain size on the drag results for a fluidized bed, the current study looks to draw conclusions about the effect of particle translation and rotation on the fluid–particle drag force that are applicable to essentially homogeneous systems. Thus, we focus on studying the dynamics of fluidized beds with a cubic periodic domain size of $n_x = 6d_p$, and then look to form conclusions that can be extended to homogeneous systems.

3.2.2. *Effect of grid resolution on the dynamics of fluidized beds*

In order to assess the sensitivity of the simulation dynamics of the fluidized bed to changes in the grid resolution, the drag curve is determined for a fluidized bed for several different grid resolutions. Keeping ν_f fixed at a value of 0.1, the effect of grid resolution on the fluid–particle drag force is assessed by analysing systems with three different particle diameters: $d_p = 8$, 12 and 18. The results of this grid resolution study are shown in figure 4, where F is plotted as a function of ϕ for a $St = 11.5$ fluidized bed. From figure 4, we observe that there is a very small difference in drag between

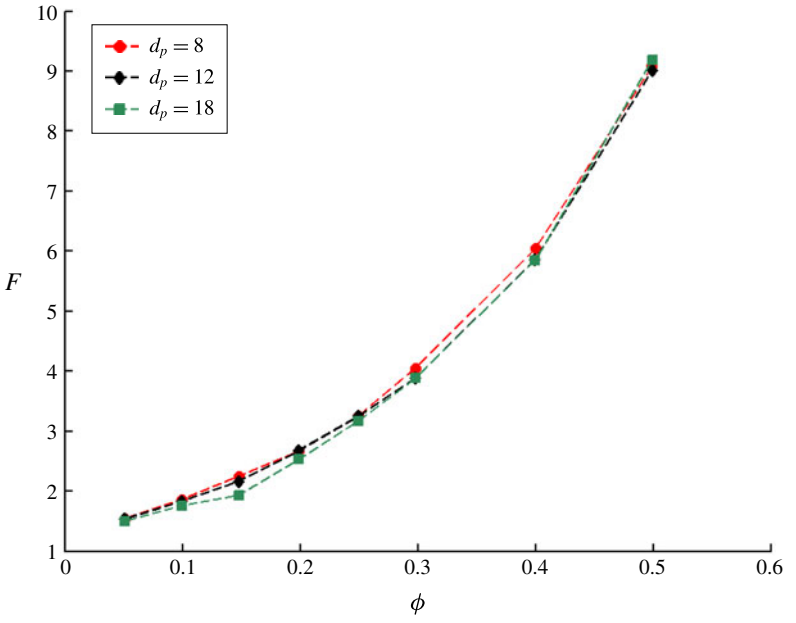

FIGURE 4. (Colour online) F is computed over a range of domain-averaged particle volume fractions, ϕ, for a $St = 11.5$ fluidized bed for three different grid resolutions (or particle diameters): $d_p = 8$, 12 and 18. For all of these cases, $\nu_f = 0.1$. From this grid sensitivity analysis, a small difference between the $d_p = 12$ and $d_p = 18$ drag curves is observed. Therefore, a value of $d_p = 12$ is taken to provide a sufficient amount of grid resolution for the current study.

the $d_p = 12$ and $d_p = 18$ cases. Thus, we conclude from this grid sensitivity analysis that a value of $d_p = 12$ provides a sufficient amount of resolution. System parameters of $d_p = 12$ and $\nu_f = 0.1$ are used for the remainder of this study.

3.2.3. *Comparison of the drag curve for the high-St limit and fluidized beds*

In figure 5, the results for F as a function of ϕ for a $St = 11.5$ fluidized bed are compared with the high-St limit (fixed-particle bed) drag values. From figure 5, the drag values for the $St = 11.5$ fluidized bed are clearly smaller than those for the high-St limit case. This drag reduction in the fluidized bed relative to the fixed bed is due to a combination of two factors: the ability of the particles to translate and rotate due to the effects of the surrounding fluid, and the development of inhomogeneities in the particle configuration. Through this work, we look to better understand each of these effects on the drag force.

3.3. *Effect of particle translation and rotation: high-St versus low-St limit*

The extent to which the particles are able to translate and rotate in response to the effects of the surrounding fluid decreases as St increases. As discussed in § 3.1, the fixed-particle bed represents the high-St limit case. At the other extreme is the low-St limit case, for which the linear and angular velocities of the particles evolve much faster than the particle positions, as discussed in § 2.2.2. The drag curve for the low-St limit case is determined using simulations, in which the configuration of particles

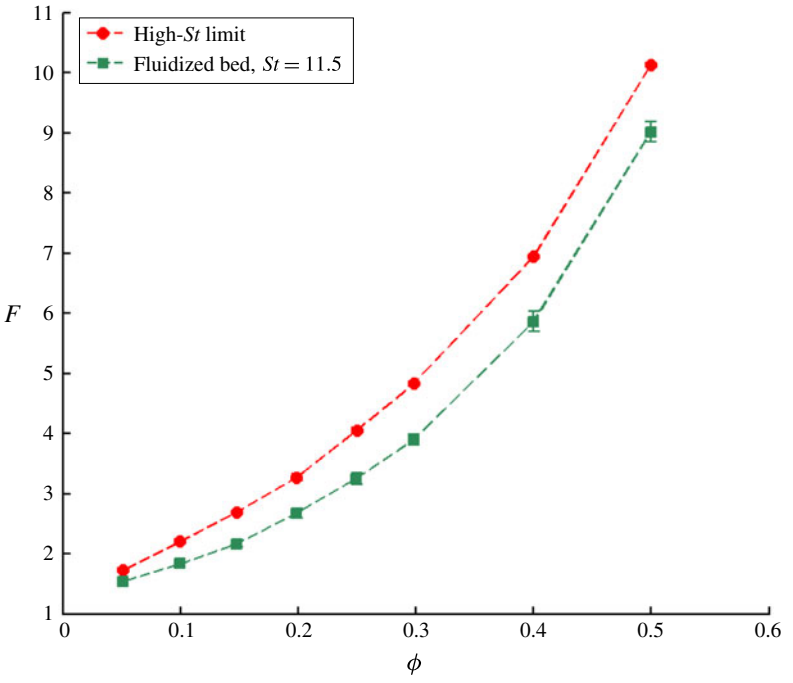

FIGURE 5. (Colour online) The drag values, F, over a range of ϕ are compared for a $St = 11.5$ fluidized bed and a high-St limit (fixed-particle) bed. For both sets of simulations, the following set of parameters are used: $d_p = 12$, $v_f = 0.1$ and $n_x = 6d_p$. It is found that there is a drag reduction going from the high-St limit curve to the fluidized bed curve.

is random, homogeneous and static. In order to ensure that there is no bias from the particle configurations when comparing the results of the low-St limit with those of the high-St limit, the same random configurations that were obtained using DEM simulations for the high-St limit case are used for the low-St limit case. Like the high-St simulations, the low-St simulations are conducted over a wide range of ϕ values. For each value of ϕ, the results are averaged over a large number (between 10 and 60) of random, homogeneous particle configurations. Since the particles are held at their initial positions and all of the simulations are conducted in the low-Re regime, the low-St drag results are independent of f_{ext} and ρ_p/ρ_f.

3.3.1. *Effect of domain size on the low-St limit simulations*

We start by analysing the effect of the domain size on the fluid–particle drag in the low-St limit case. In figure 6, the results for F as a function of ϕ are presented for three different cubic periodic domain sizes: $n_x = 6d_p$, $9d_p$ and $12d_p$. From figure 6, there is a clear reduction in drag in the low-St limit case as the domain size increases. In contrast to the fluidized bed case, as an equilibrium velocity profile is established in the low-St limit simulations, the development of flow-induced inhomogeneities is suppressed by keeping the particles fixed in place. Thus, the effects of periodicity (or domain size) can be eliminated by extrapolating the low-St limit drag results to an infinite domain size. Using a $1/n_x$ dependence, as shown in the inset of figure 6 for the $\phi = 0.3$ case, the drag results are extrapolated to an infinite domain size ($n_x \to \infty$). While the drag curve given by (1.6) has a constant exponent, n, the $n_x \to \infty$ drag

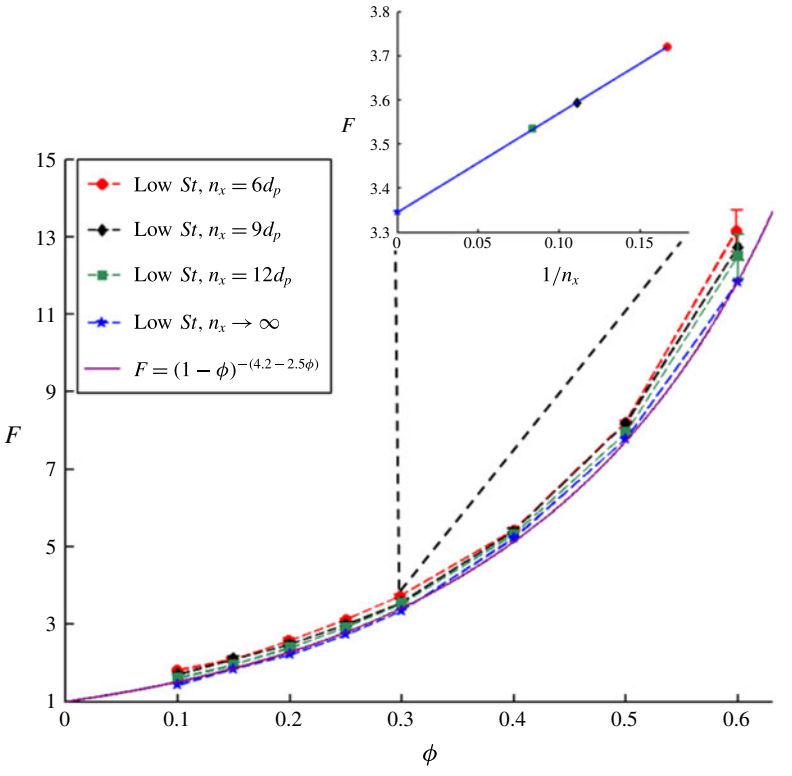

FIGURE 6. (Colour online) F is computed over a range of domain-averaged particle volume fractions, ϕ, for a low-St limit bed for three different cubic periodic domain sizes: $n_x = 6d_p$, $9d_p$ and $12d_p$. System parameters of $d_p = 12$ and $\nu_f = 0.1$ are used for all of these simulations. Using a $1/n_x$ dependence, these results are extrapolated to an infinite domain size ($n_x \to \infty$), as shown in the inset for the case $\phi = 0.3$. The drag curve for the $n_x \to \infty$ low-St limit matches very closely the drag curve (1.6) of Wen & Yu (1966) type, with a ϕ-dependent exponent: $n(\phi) = 6.2 - 2.5\phi$.

results are best fitted with an exponent that varies with ϕ: $n(\phi) = 6.2 - 2.5\phi$. Outside the dilute limit, this value of n primarily lies in the range 4.65–5.5 given by the sedimentation experiments of Richardson & Zaki (1954), Wen & Yu (1966) and Garside & Al-Dibouni (1977). Furthermore, this drag curve has a similar form to the analytical approximation of Brady & Durlofsky (1988) for the hindered sedimentation velocity. Such a result confirms that the low-St limit simulations indeed provide an accurate depiction of the fluid–particle interactions in liquid–solid sedimentation.

3.3.2. *High-St limit versus low-St limit*

As discussed in § 3.2.1, our goal is to form conclusions about the dynamics of fluid–particle interactions that can be extended to nearly homogeneous systems by using periodic simulation cells of domain size $n_x = 6d_p$. Towards this goal, we compare the high-St and low-St drag curves using results obtained from simulation cells of domain size $n_x = 6d_p$. These results for F as a function of ϕ are shown in figure 7, where we observe a significant reduction in drag when moving from the high-St limit curve to the low-St limit curve. This drag reduction ranges from 10 % for $\phi = 0.05$ to 19 %

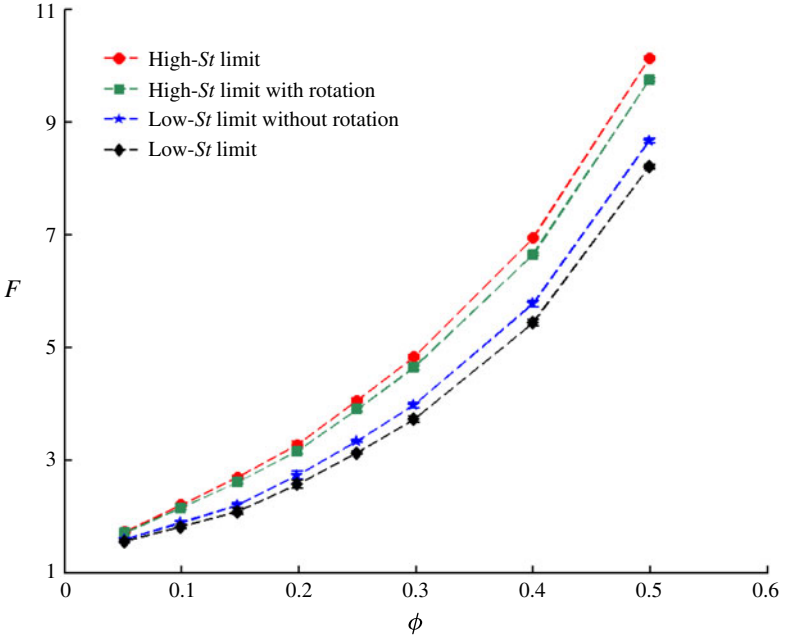

FIGURE 7. (Colour online) F as a function of ϕ is compared for (1) the high-St limit case, (2) the high-St limit case with particle rotation, (3) the low St limit case without particle rotation and (4) the low-St limit case. The results for all of these cases are taken from periodic cells with a domain size of $n_x = 6d_p$. In order to ensure that there is no bias due to the configuration of particles, all four cases use the same random, homogeneous particle configurations. It is clear that the low-St limit case has the lowest drag over the entire range of ϕ. This drag reduction on moving from the high-St limit to the low-St limit is due to the evolution of the linear and angular velocities of the low-St limit particles in response to the fluid velocity field.

for $\phi = 0.5$. Since the high- and low-St limit cases are both simulated using identical random, homogeneous particle configurations, this drag reduction is not a result of changes in the extent of inhomogeneities. Instead, this drag reduction is due to the evolution of the linear and angular velocities of the particles in response to the effects of the surrounding fluid in the low-St limit case. Since the low-St limit particles are able to adapt to the fluid velocity field, there is less fluid–particle drag in the low-St limit case when compared with the high-St limit case, where the particles are not able to adjust at all to the effects of the surrounding fluid. From this analysis, we conclude that for any given particle configuration in the low-Re regime, the high-St limit case maximizes the fluid–particle drag in the system, while the low-St limit case minimizes the drag. Figure 7 is analogous to figure 1 where the curve of van der Hoef *et al.* (2005) is compared with that of Wen & Yu (1966).

In figure 7, the drag results for two additional hypothetical cases are shown: high-St limit with particle rotation (to achieve zero net torque) and low-St limit without particle rotation. Due to the ability of the particles to rotate in response to the surrounding fluid in the case of the high-St limit with rotation, there is a small reduction in drag when compared with the case of the regular high-St limit. This drag reduction ranges from 1 % for $\phi = 0.05$ to 4 % for $\phi = 0.5$. Furthermore, when the particles are not allowed to rotate in the low-St limit, there is a small increase

in drag when compared with the case of the regular low-St limit. This increase in drag ranges from 2 % for $\phi = 0.05$ to 6 % for $\phi = 0.5$. Thus, the difference in F between the high-St and low-St limits is mostly due to the ability of the particles in the latter case to attain non-zero translational velocity in order to achieve zero net force. In the Appendix, further details of the impact of particle velocity fluctuations on drag are given. It is demonstrated there that in the low-St limit, the fluctuations are coherent and lead to a reduction of drag as compared to fixed beds (i.e. the high-St limit). It is also shown that random, uncorrelated velocity fluctuations do not induce a drag-reducing effect.

3.4. *Effect of flow-induced inhomogeneities*

In order to assess the importance of flow-induced inhomogeneities on the fluid–particle drag, we isolate the effects of inhomogeneities from that of particle translation and rotation by simulating high- and low-St limit beds using what we refer to as 'frozen' fluidized particle configurations. These 'frozen' configurations are obtained by taking a snapshot from a fluidized bed simulation long after a statistical steady state has been reached. Due to the formation of particle clusters and voids in the fluidized beds, these 'frozen' configurations are inhomogeneous. High-St and low-St limit simulations are then conducted using these inhomogeneous configurations. The same set of inhomogeneous configurations are used for both the high- and low-St limit cases. In figure 8, the results of F over a range of ϕ for the inhomogeneous high-St (figure 8*a*) and low-St (figure 8*b*) limit cases are compared with their respective values taken from random, homogeneous configurations. The inhomogeneous configurations are taken from fluidized beds with $St = 11.5$. In the high-St limit case (figure 8*a*), when moving from the homogeneous curve to the inhomogeneous curve, there is a small but noticeable reduction in drag at lower particle volume fractions ($\phi < 0.3$), and no change in drag as the packing fraction approaches the close packing limit ($\phi > 0.3$). From these results, the development of inhomogeneities appears to be hindered at higher particle volume fractions. In the low-St limit case (figure 8*b*), when moving from the homogeneous curve to the inhomogeneous curve, there is a significant reduction in drag over the entire range of ϕ. Thus, it appears that inhomogeneities in the particle configuration have a stronger effect on the fluid–particle drag when the particle velocities are able to adjust to the effects of the surrounding fluid. Overall, inhomogeneities have a noticeable effect on the fluid–particle interactions, and must therefore be accounted for when devising a drag model.

The goal of this study is to obtain a drag model that can be applied to larger-scale numerical studies of fluidized beds. For studies of this type, the drag relations are typically applied at length scales over which the particle configuration is taken to be approximately homogeneous. Therefore, we seek to obtain a drag relation that is applicable to fluidized beds with homogeneous particle configurations. To achieve this goal, we need to isolate the effects of particle translation and rotation from the effects of inhomogeneities.

3.5. *Quantification of relative fluidized bed behaviour*

In order to isolate the effect of particle translation and rotation from the effect of inhomogeneities, we compare the dimensionless drag curves taken from the following three systems: (1) $St = St_{given}$ fluidized bed, (2) the high-St limit bed that uses the inhomogeneous configuration of particles taken from snapshots of the St_{given} fluidized bed, and (3) the low-St limit bed that uses the inhomogeneous configuration of particles also taken from the St_{given} fluidized bed. In doing so, we are comparing these three different types of systems by taking drag data from snapshots that contain

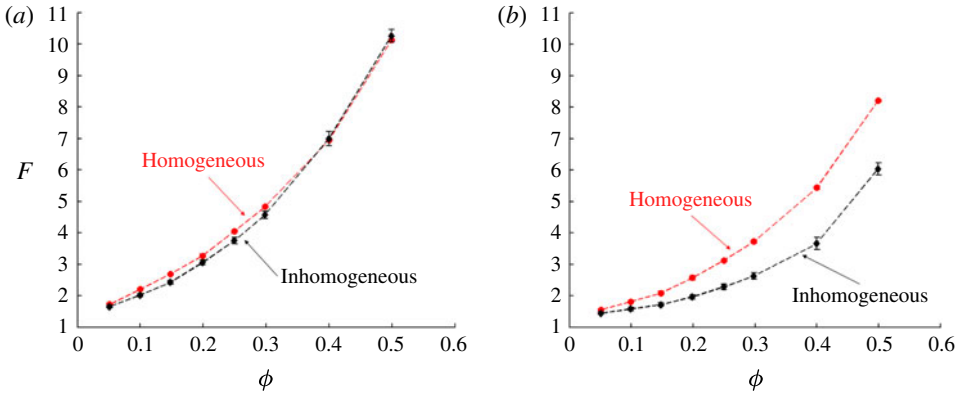

FIGURE 8. (Colour online) The values of F over a range of ϕ taken from the 'frozen', inhomogeneous fluidized configurations are compared with values taken from a random, homogeneous configuration for both (*a*) the high-*St* limit case and (*b*) the low-*St* limit case. The inhomogeneous configurations are obtained by taking snapshots of $St = 11.5$ fluidized beds long after a statistical steady state has been achieved. In the high-*St* limit case, when moving from the homogeneous curve to the inhomogeneous curve, there is a small reduction in drag in the range $\phi < 0.3$, and no effect on the drag in the range $\phi > 0.3$. In the low-*St* limit case, the inhomogeneous drag curve is significantly lower than the homogeneous curve over the entire range of ϕ. Overall, the effects of inhomogeneities tend to result in a drag reduction.

identical configurations of particles. Thus, the observed differences in the drag values are solely a result of the differences in the abilities of the particles to translate and rotate. In figure 9, these three drag curves are shown for particle configurations taken from $St = 11.5$ fluidized bed simulations. We see that, as expected, the high-*St* limit case maximizes the drag, while the low-*St* limit case minimizes the drag for any given configuration. The drag for the fluidized bed lies in between these two limits over the full range of ϕ.

The relative behaviour of the fluidized bed compared with the high- and low-*St* limit cases is quantified using the ratio α, which we define as

$$\alpha = \frac{F_{fluidized} - F_{low\,St,\,inhom}}{F_{high\,St,\,inhom} - F_{low\,St,\,inhom}}. \tag{3.1}$$

Since the high- and low-*St* limit cases provide the two limiting values for the drag, $0 \leqslant \alpha \leqslant 1$. For a fluidized bed exhibiting low-*St* limit behaviour, $\alpha = 0$, and for a fluidized bed exhibiting high-*St* limit behaviour, $\alpha = 1$.

3.6. *Using α to define a new drag model*

Using the method shown in figure 9 and (3.1), α is computed over a range of ϕ, ρ_p/ρ_f, *Re* and *St*. A sample of these results is presented in table 1. From the first two rows of data in table 1, it is clear that when two different systems have the same ϕ and *Re*, but have a different ρ_p/ρ_f, the value of α is different. Furthermore, by comparing the third and fourth rows of table 1, it is clear that when two different systems have the same ϕ and ρ_p/ρ_f, but have different values of *Re*, the value of α is different. Finally, by comparing the fourth and fifth rows of data in table 1, it appears that when two

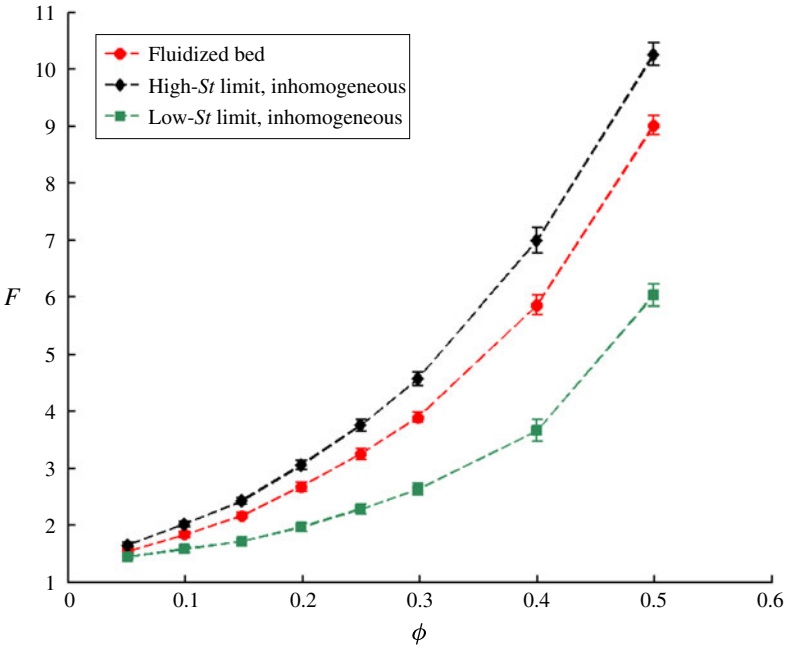

FIGURE 9. (Colour online) The drag values, F, as a function of ϕ are shown for three different system types: (1) the $St = 11.5$ fluidized bed, (2) the high-St limit bed using inhomogeneous particle configurations taken from snapshots of the $St = 11.5$ fluidized bed, and (3) the low-St limit using inhomogeneous particle configurations taken from snapshots of the $St = 11.5$ fluidized bed. There is a reduction in drag going from the high-St limit case to the fluidized bed case to the low-St limit case due to the effects of particle translation and rotation.

ϕ	ρ_p/ρ_f	Re	St	α
0.1	4	0.25	0.056	0.0034
0.1	1500	0.25	21	0.68
0.2	300	0.17	2.8	0.36
0.2	300	0.31	5.2	0.49
0.2	600	0.16	5.2	0.47

TABLE 1. The results for α for several different types of fluidized beds.

different systems have the same ϕ and St, but different values of ρ_p/ρ_f and Re, the value α is nearly the same. Thus, $\alpha = \alpha(\phi, St)$.

In figure 10, α is plotted as a function of St for domain-averaged particle volume fractions, ϕ, ranging from 0.1 to 0.4. For each curve of α versus St, three distinct regimes are observed: (1) the low-St regime, where $\alpha \to 0$ as $St \to 0$; (2) the intermediate-St regime, where there is a gradual increase in α as St increases; and (3) the high-St regime, where $\alpha \to 1$ as $St \to \infty$. Thus, we see that α describes the transition from the low-St regime to the high-St regime. As ϕ increases, the transition from the low-St regime to the high-St regime occurs at lower values of St. The reason for this is that at higher values of ϕ, the fluidized bed tends to behave more like a

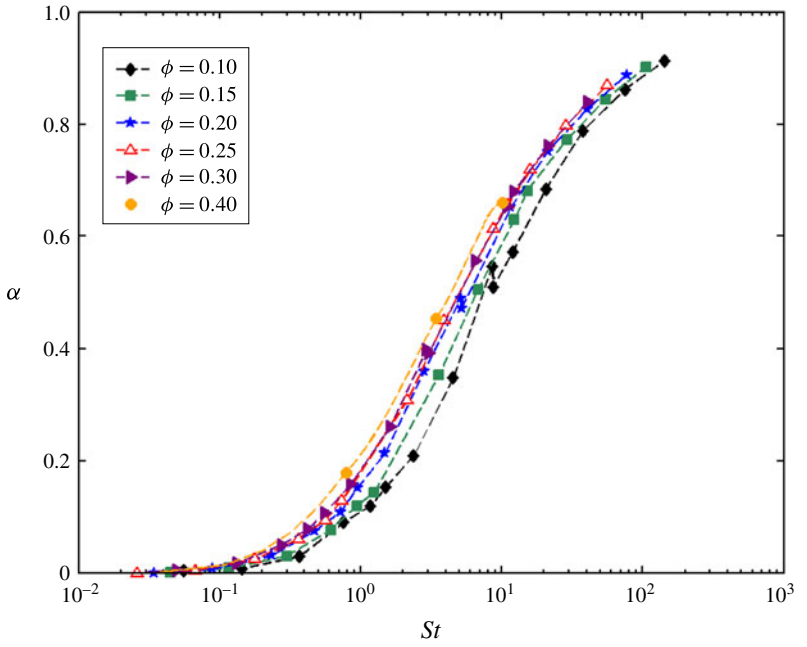

FIGURE 10. (Colour online) α is plotted as a function of St over a wide range of ϕ. The simulation results are taken from a periodic domain size of $n_x = 6d_p$. For each value of ϕ, three distinct regimes are observed: (1) the low-St regime ($\alpha \to 0$ as $St \to 0$), (2) intermediate-St regime (α gradually increases as St increases) and (3) high-St regime ($\alpha \to 1$ as $St \to \infty$). Furthermore, as ϕ increases, the fluidized bed tends to behave more like a packed bed, and so the transition to a high-St limit type of behaviour occurs at lower values of St.

packed bed, and so the transition to a high-St limit type of behaviour occurs at lower values of St.

Analysing the results of figure 10, we see that we can collapse the curves of α versus St onto a single curve by using a modified Stokes number, $\tilde{St}$, which is defined as

$$\tilde{St} = \frac{St}{(1-\phi)^2}, \tag{3.2}$$

with St defined as in (1.7). The results of α as a function of $\tilde{St}$ for a wide range of ϕ are shown in figure 11. The exponent of 2 in (3.2) provides the most complete collapse of the α versus St data onto a single curve, and seems to capture the effect of higher packing fractions hindering the free translation and rotation of particles, causing the flow to transition to the high-St limit at lower values of St for more packed-bed-like cases (higher values of ϕ). Thus, for a domain size of $n_x = 6d_p$, α is solely a function of $\tilde{St}$.

3.6.1. *Effect of domain size on* α

The effect of the domain size on α as a function of $\tilde{St}$ is shown in figure 12. In figure 12, we see that even as the system size is changed from $n_x = 6d_p$ to $n_x = 9d_p$ to $n_x = 12d_p$, the curve of α as a function of $\tilde{St}$ remains approximately unchanged.

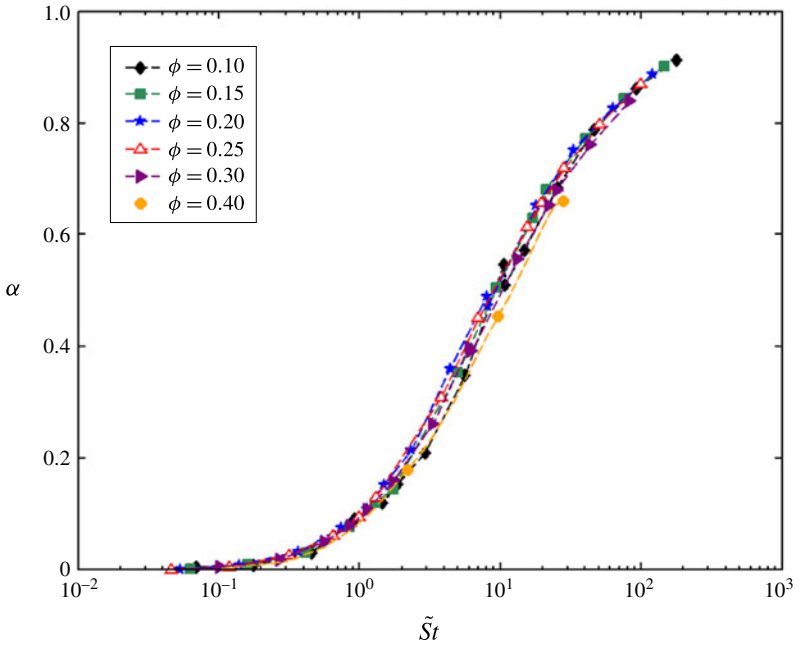

FIGURE 11. (Colour online) α is plotted as a function of $\tilde{St}$ over a wide range of ϕ values. The choice of $\tilde{St} = St/(1-\phi)^2$ allows all of the α curves to collapse onto a single curve. For a domain size of $n_x = 6d_p$, α is solely a function of $\tilde{St}$.

As the size of the system size increases, the extent to which the particles are able to form structures increases, and so the extent of inhomogeneities increases. Despite the fact that the domain size of our periodic system has an effect on the development of flow structures and on the distribution of particles, we have developed a method for characterizing the extent to which particles are able to translate and rotate that is independent of the domain size. Thus, we have found that $\alpha(\tilde{St})$ is applicable to nearly homogeneous systems. A simple curve that follows the shape of $\alpha(\tilde{St})$ is given by

$$\alpha(\tilde{St}) = \frac{1}{2}\left(1 + \frac{\tilde{St} - 10}{\tilde{St} + 10}\right). \tag{3.3}$$

The form of (3.3) appears to suggest that $\tilde{St} = 10$ is the centre point for the intermediate-St regime. For $\tilde{St} < 1$, the fluid–particle system is in the low-St regime, while for $\tilde{St} > 100$, the system is in the high-St regime.

From figure 12, we see that with the use of this α analysis, we have successfully formed conclusions about the fluid–particle interactions that are applicable to nearly homogeneous systems. We have observed a dependence of $\tilde{St}$ on the fluid–particle drag force, primarily using simulation systems with a domain size of $n_x = 6d_p$, that remains valid even as the domain size changes. Such conclusions are particularly powerful in that they allow us to study the dynamics of the fluid–particle interactions with the use of a relatively small number of particles.

As discussed in § 3.4, the goal of this study is to obtain a constitutive relation for the fluid–particle drag force that is applicable to larger-scale simulations of fluid–

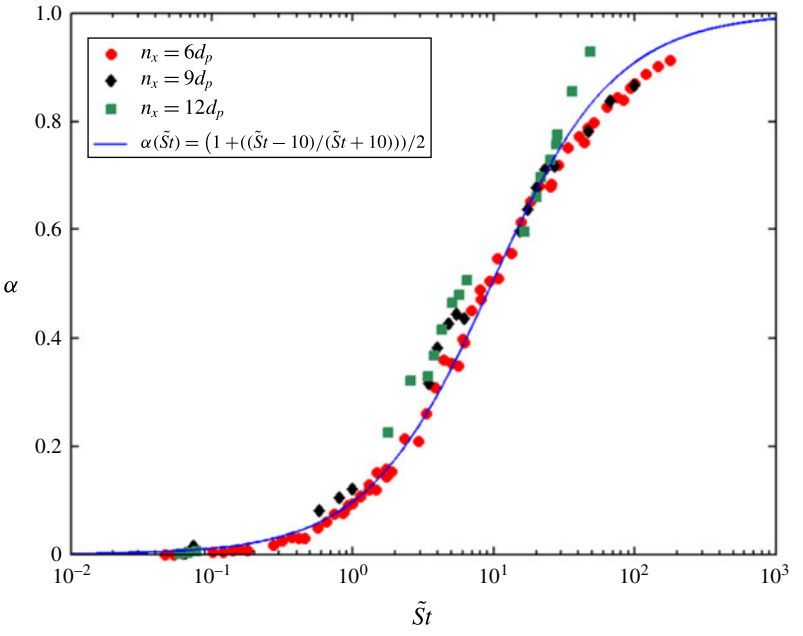

FIGURE 12. (Colour online) α is plotted as a function of $\tilde{St}$ for domain sizes of $6d_p$, $9d_p$ and $12d_p$. From this curve, we see that $\alpha(\tilde{St})$ does not vary significantly with the domain size. A single fitted curve is then used to describe this $\alpha(\tilde{St})$ curve. The results shown in this plot are taken from a large range of ϕ.

particle systems. In these larger-scale simulations, the particle configuration is typically taken to be approximately homogeneous at the scale of the fluid grid size, and so we seek a drag model that is applicable to homogeneous configurations, which we denote as $F_{fluidized,hom}$. Because $\alpha(\tilde{St})$ does not vary with n_x, we can extrapolate the results to a system where the particle configuration is homogeneous:

$$\alpha(\tilde{St}) = \frac{F_{fluidized} - F_{low\,St,\,inhom}}{F_{high\,St,\,inhom} - F_{low\,St,\,inhom}} = \frac{F_{fluidized,hom} - F_{low\,St,\,hom}}{F_{high\,St,\,hom} - F_{low\,St,\,hom}}. \tag{3.4}$$

Rearranging the terms in (3.4), we find that in the low-Re regime, the drag relation, which is applicable to homogeneous particle distributions, is given by

$$F(\phi, St) = F_{fluidized,hom} = \alpha(\tilde{St})F_{high\,St,\,hom}(\phi) + (1 - \alpha(\tilde{St}))F_{low\,St,\,hom}(\phi). \tag{3.5}$$

Since, in the low-Re regime, $F_{high\,St,\,hom} = F_{van\,der\,Hoef}$ and $F_{low\,St,\,hom} = (1-\phi)^{-(n(\phi)-2)}$, (3.5) can be re-expressed as

$$F(\phi, St) = \alpha(\tilde{St})F_{van\,der\,Hoef}(\phi) + (1 - \alpha(\tilde{St}))(1-\phi)^{-(n(\phi)-2)}, \tag{3.6}$$

where $\alpha(\tilde{St})$ is given by (3.3), $F_{van\,der\,Hoef}(\phi)$ is given by (1.5) and $n(\phi) = 6.2 - 2.5\phi$, as shown in figure 6. In (3.6), we have proposed a new drag model, which is dependent on both ϕ and St.

As shown in figure 13, the new drag relation is able to bridge the gap between the low-St type models, like that of Wen & Yu (1966), and the high-St type models,

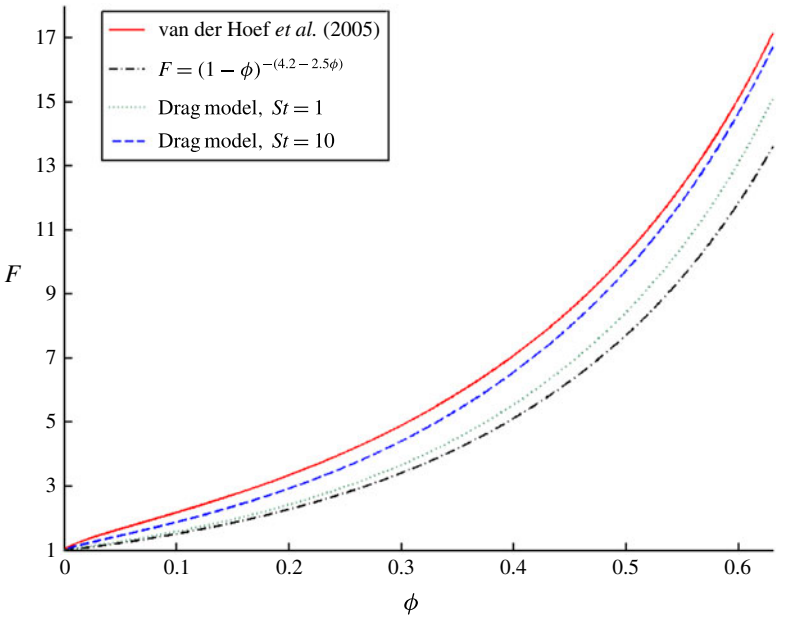

FIGURE 13. (Colour online) The proposed drag model (3.6) is shown with a plot of the dimensionless drag force, F, as a function of ϕ, for both $St = 1$ and $St = 10$. These drag curves are compared with the curve of van der Hoef *et al.* (2005) and with the drag curve of Wen & Yu (1966) type, $F = (1-\phi)^{-(n(\phi)-2)}$, with $n(\phi) = 6.2 - 2.5\phi$.

like that of van der Hoef *et al.* (2005), and is applicable over a full range of St in the low-Re regime. This bridging property of the proposed drag model represents a significant improvement on prior drag relations, because this new model is able to more fully capture the effect of particle mobility on the fluid–particle interactions. In figure 13, the proposed drag model is shown for both $St = 1$ and $St = 10$ with F as a function of ϕ. As expected, the $St = 10$ drag is higher than the $St = 1$ drag. When comparing these curves with the curve of van der Hoef *et al.* (2005) and a drag curve of Wen & Yu (1966) type, $F = (1-\phi)^{-(n-2)}$ with $n(\phi) = 6.2 - 2.5\phi$, we see that there is a significant difference between the predictions given by the new drag relation and those given by traditional models (Wen & Yu 1966; van der Hoef *et al.* 2005) and hybrid models (Gidaspow 1994) that are simply equal to the curve of Wen & Yu (1966) type at low ϕ and equal to that of van der Hoef *et al.* (2005) type at high ϕ. Thus, in the low-Re regime, unlike prior drag models, the proposed drag model (3.6) is able to describe the fluid–particle drag force over a full range of St and ϕ.

4. Summary

Through this work, a new drag model (3.6) has been proposed that, unlike previous drag models, is a function of both ϕ and St in the low-Re regime. Prior LBM drag studies have developed models for the fluid–particle drag force that are valid over the entire range of ϕ, but are only applicable to high-St systems. Furthermore, prior hybrid drag models, like that of Gidaspow (1994), have blended fixed-bed (for high ϕ) and sedimentation (for low ϕ) drag models, but have implicitly assumed that fluid–particle systems exhibit high-St behaviour at high ϕ and low-St behaviour at low ϕ. We have found that such a simplification is not accurate over a full range of St. In

the current work, we have developed a drag model that provides a smooth blending of the packed-bed and sedimentation drag models over both ϕ and St. This new drag model bridges the transition from low ϕ to high ϕ, as well as from low St to high St. By accounting for the effect of particle translation and rotation on the interactions between the fluid and particles, this St-dependent drag relation is able to capture a wider range of fluid and particle properties than was previously attainable through the drag models available in the literature.

The current drag model is constructed using LBM simulations with a cubic periodic domain. For larger-scale simulations of fluid–particle systems, the fluid grid size is larger than the particle diameter, and so the fluid–particle drag force cannot simply be computed by summing the forces over the surface of the particle, as is done in the case of LBM. Instead, the fluid–particle drag force is determined from an input constitutive relation. Since the distribution of particles is typically taken to be approximately homogeneous at the fluid grid scale, the drag model derived in the current work must be applicable to the homogeneous configuration in order for it to be used as a constitutive relation in the larger-scale simulations. Using a combination of fluidized, fixed and low-St limit bed simulations, the methodology for obtaining the drag relation is successfully extrapolated to a homogeneous system. Thus, a drag model that is applicable to homogeneous particle distributions is obtained.

In summary, we have presented a framework for developing drag laws based on ϕ and St. While the current analysis is for low-Re systems, this methodology can be extended to higher values of Re. Through its application to larger-scale numerical models of fluidized beds, this new drag relation has the potential to increase the quantitative precision of these models, and thus widen our understanding of a range of industrial processes.

Acknowledgements

This work is supported by a grant from the ExxonMobil Research & Engineering Co., and by a fellowship awarded to G.J.R. by the National Science Foundation (DGE-1148900).

Appendix. Effect of velocity fluctuations in the low-Re regime

The validity of the low-Re fixed-bed simulations is further probed by analysing the effect of fluctuations in the angular and linear particle velocities on the drag force. The strength of the fluctuations in $\boldsymbol{v}_p$ is characterized by Re_T (2.17), while the strength of the fluctuations in $\boldsymbol{\Omega}_p$ is characterized by Re_Ω (2.18). In the homogeneous low-St limit simulations, particles attain non-zero values of $\boldsymbol{v}_p$ and $\boldsymbol{\Omega}_p$, such that the net force and torque on each particle are 0. In this low-St limit case, $Re_T \approx 0.05$ and $Re_\Omega \approx 0.06$. Although Re, Re_T, $Re_\Omega \ll 1$ in the low-St limit case, there is a significant reduction (between 10 % and 20 %) in drag when compared with the case of a fixed bed (high-St limit), as discussed in § 3.3.2. The reason for this drag reduction is that while the fluctuations in $\boldsymbol{v}_p$ and $\boldsymbol{\Omega}_p$ are small, they are not random. There is a clear correlation in the particle velocity fluctuations based on their locations within the flow, as shown in figure 14(a,b). These correlated velocity fluctuations in the low-St limit case act to reduce the drag of the fluid flow past the homogeneous array of particles.

Since Re, Re_T, $Re_\Omega \ll 1$, the low-St limit case with f_{ext} and non-zero values of $\boldsymbol{v}_p = \boldsymbol{v}_{p,\,low\,St}$ and $\boldsymbol{\Omega}_p = \boldsymbol{\Omega}_{p,\,low\,St}$ can be broken into a superposition of the following three systems: (1) a fixed bed with f_{ext}, and zero $\boldsymbol{v}_p$ and $\boldsymbol{\Omega}_p$; (2) a system with zero f_{ext} and $\boldsymbol{\Omega}_p$, and $\boldsymbol{v}_p = \boldsymbol{v}_{p,\,low\,St}$; and (3) a system with zero f_{ext} and $\boldsymbol{v}_p$, and $\boldsymbol{\Omega}_p = \boldsymbol{\Omega}_{p,\,low\,St}$. By simulating each of these subsystems, we found that such a superposition is valid

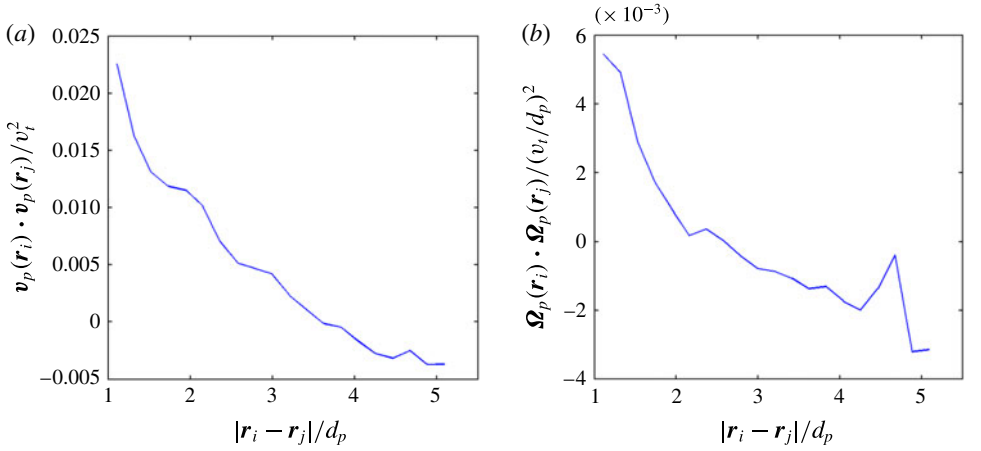

FIGURE 14. (Colour online) The correlations of fluctuations in (*a*) $\boldsymbol{v}_p$ and (*b*) $\boldsymbol{\Omega}_p$ in the low-*St* limit case with particle separation distance are shown. In these plots, the subscripts i and j designate two different particles in the system, while v_t is the terminal particle velocity and $\boldsymbol{r}_i$ is the position of particle i. There is a clear positive correlation in both $\boldsymbol{v}_p$ and $\boldsymbol{\Omega}_p$ at small particle distances, which signifies that the velocity fluctuations in the low-*St* limit case are not random.

by confirming that $\boldsymbol{u}_{s,\,low\,St} = \boldsymbol{u}_{s,\,case\,1} + \boldsymbol{u}_{s,\,case\,2} + \boldsymbol{u}_{s,\,case\,3}$. This result demonstrates that the fluctuations in $\boldsymbol{v}_p$ and $\boldsymbol{\Omega}_p$ in the low-*St* limit case are indeed small. Furthermore, we observe that the small, correlated values of $\boldsymbol{v}_p$ and $\boldsymbol{\Omega}_p$ in cases (2) and (3), respectively, produce a mean flow (non-zero value of $\boldsymbol{u}_s$) even in the absence of an external force, f_{ext}.

Next, we look to investigate the effect of small, random fluctuations in $\boldsymbol{v}_p$ and $\boldsymbol{\Omega}_p$, with intensities equivalent to that of the correlated fluctuations in the low-*St* case: $Re_T \approx 0.05$ and $Re_\Omega \approx 0.06$, respectively. We study these random fluctuations via the following four systems: (1) a system with f_{ext} and random fluctuations in $\boldsymbol{v}_p$; (2) a system with f_{ext} and random fluctuations in $\boldsymbol{\Omega}_p$; (3) a system with zero f_{ext} and random fluctuations in $\boldsymbol{v}_p$; and (4) a system with zero f_{ext} and random fluctuations in $\boldsymbol{\Omega}_p$. In each case, the velocity value imposed on each particle is chosen at random from a Gaussian distribution. We find that the dimensionless drag force, F, for case (1) is nearly equivalent to that of the fixed bed. In fact, these drag values differ by just 0.02 % at $\phi = 0.3$ and by 0.67 % at $\phi = 0.25$. Similarly, we find that the values of F for case (2) are equivalent to within 0.1 % to that of the fixed bed. Since Re, $Re_T, Re_\Omega \ll 1$ in both of these cases, the contribution of the random fluctuations to the overall fluid–particle drag force is, as expected, negligible. Additionally, in simulating cases (3) and (4), we find that the small, random (uncorrelated) values of $\boldsymbol{v}_p$ and $\boldsymbol{\Omega}_p$ are unable to produce a mean flow in the absence of f_{ext}. These sets of simulations further confirm the validity of the LBM scheme in the low-*Re* regime.

REFERENCES

AIDUN, C. K. & CLAUSEN, J. R. 2010 Lattice-Boltzmann method for complex flows. *Annu. Rev. Fluid Mech.* **42**, 439–472.

BEETSTRA, R., VAN DER HOEF, M. A. & KUIPERS, J. A. M. 2007 Drag force of intermediate Reynolds number flow past mono- and bi-disperse arrays of spheres. *AIChE J.* **52** (2), 489–501.

BENZI, R., SUCCI, S. & VERGASSOLA, M. 1992 The lattice Boltzmann equation: theory and applications. *Phys. Rep.* **222** (3), 145–197.

BRADY, J. F. & DURLOFSKY, L. J. 1988 The sedimentation rate of disordered suspensions. *Phys. Fluids* **31** (4), 717–727.

BRINKMAN, H. C. 1947 A calculation of the viscous force exerted by a flowing fluid on a dense swarm of particles. *Appl. Sci. Res.* **A1**, 27–34.

CARMAN, P. C. 1937 Fluid flow through granular beds. *Trans. Inst. Chem. Engrs* **15**, 150–166.

TEN CATE, A., NIEUWSTAD, C. H., DERKSEN, J. J. & VAN DEN AKKER, H. E. A. 2002 Particle imaging velocimetry experiments and lattice-Boltzmann simulations on a single sphere settling under gravity. *Phys. Fluids* **14** (11), 4012–4025.

CHEN, S. & DOOLEN, G. D. 1998 Lattice Boltzmann method for fluid flows. *Annu. Rev. Fluid Mech.* **30**, 329–364.

DARCY, H. P. G. 1856 *Les fontanes publiques de la ville de Dijon*. Dalmont.

DAVIS, R. H. & ACRIVOS, A. 1985 Sedimentation of noncolloidal particles at low Reynolds numbers. *Annu. Rev. Fluid Mech.* **17**, 91–118.

DERKSEN, J. J. & SUNDARESAN, S. 2007 Direct numerical simulations of dense suspensions: wave instabilities in liquid–fluidized beds. *J. Fluid Mech.* **587**, 303–336.

DERKSEN, J. J. & VAN DEN AKKER, H. E. A. 1999 Large-eddy simulations on the flow driven by a Rushton turbine. *AIChE J.* **45**, 209–221.

EGGELS, J. G. M. & SOMERS, J. A. 1995 Numerical simulation of free convective flow using the lattice-Boltzmann scheme. *Intl J. Heat Fluid Flow* **16** (5), 357–364.

ERGUN, S. 1952 Fluid flow through packed columns. *Chem. Engng Prog.* **48** (2), 89–94.

GARSIDE, J. & AL-DIBOUNI, M. R. 1977 Velocity-voidage relationships for fluidization and sedimentation in solid–liquid systems. *Ind. Engng Chem. Process Des. Dev.* **16**, 206–214.

GIDASPOW, D. 1994 *Multiphase Flow and Fluidization: Continuum and Kinetic Theory Descriptions*. Academic.

GOLDSTEIN, D., HANDLER, R. & SIROVICH, L. 1993 Modeling a no-slip flow boundary with an external force field. *J. Comput. Phys.* **105** (2), 354–366.

HIGUERA, F. J. & JIMENEZ, J. 1989 Boltzmann approach to lattice gas simulations. *Europhys. Lett.* **9** (7), 663–668.

HIGUERA, F. J. & SUCCI, S. 1989 Simulating the flow around a circular cylinder with a lattice Boltzmann equation. *Europhys. Lett.* **8** (6), 517–521.

HIGUERA, F. J., SUCCI, S. & BENZI, R. 1989 Lattice gas dynamics with enhanced collisions. *Europhys. Lett.* **9** (4), 345–349.

HILL, R. J., KOCH, D. L. & LADD, A. J. C. 2001 The first effects of fluid inertia on flows in ordered and random arrays of spheres. *J. Fluid Mech.* **448**, 213–241.

VAN DER HOEF, M. A., BEETSTRA, R. & KUIPERS, J. A. M. 2005 Lattice-Boltzmann simulations of low-Reynolds-number flow past mono- and bidisperse arrays of spheres: results for the permeability and drag force. *J. Fluid Mech.* **528**, 233–254.

IGCI, Y. & SUNDARESAN, S. 2011 Constitutive models for filtered two-fluid models of fluidized gas–particle flows. *Ind. Engng Chem. Res.* **50**, 13190–13201.

KIM, S. & KARILLA, S. J. 1991 *Microhydrodynamics: Principles and Selected Applications*. Butterworth-Heinemann.

KIM, S. & RUSSEL, W. B. 1985 Modelling of porous media by renormalization of the Stokes equations. *J. Fluid Mech.* **154**, 269–286.

KOCH, D. L. & SANGANI, A. S. 1999 Particle pressure and marginal stability limits for a homogeneous monodisperse gas–fluidized bed: kinetic theory and numerical simulations. *J. Fluid Mech.* **400**, 229–263.

KOZENY, J. 1927 Ueber kapillare Leitung des Wassers in Boden. *Sitz. ber. Akad. Wiss. Wien* **136** (2a), 271–306.

KRIEBITZSCH, S. H. L., VAN DER HOEF, M. A. & KUIPERS, J. A. M. 2013 Fully resolved simulation of a gas-fluidized bed: a critical test of DEM models. *Chem. Engng Sci.* **91**, 1–4.

LADD, A. J. C. 1994 Numerical simulations of particulate suspensions via a discretized Boltzmann equation. Part 1. Theoretical foundation. *J. Fluid Mech.* **271**, 285–309.

LADD, A. J. C. 1997 Sedimentation of homogeneous suspensions of non-Brownian spheres. *Phys. Fluids* **9** (3), 491–499.

LI, J. & KUIPERS, J. A. M. 2003 Gas–particle interactions in dense gas–fluidized beds. *Chem. Engng Sci.* **58**, 711–718.

MCNAMARA, G. R. & ZANETTI, G. 1988 Use of the Boltzmann equation to simulate lattice-gas automata. *Phys. Rev. Lett.* **61** (20), 2332–2335.

NGUYEN, N.-Q. & LADD, A. J. C. 2002 Lubrication corrections for lattice-Boltzmann simulations of particle suspensions. *Phys. Rev.* E **66**, 046708.

NGUYEN, N.-Q. & LADD, A. J. C. 2005 Sedimentation of hard-sphere suspensions at low Reynolds number. *J. Fluid Mech.* **525**, 73–104.

OZEL, A., FEDE, P. & SIMONIN, O. 2013 Development of filtered Euler–Euler two-phase model for circulating fluidised bed: high resolution simulation, formulation and *a priori* analyses. *Intl J. Multiphase Flow* **55**, 43–63.

PEPIOT, P. & DESJARDINS, O. 2012 Numerical analysis of the dynamics of two- and three-dimensional fluidized bed reactors using an Euler–Lagrange approach. *Powder Technol.* **220**, 104–121.

QIAN, Y. H., D'HUMIERES, D. & LALLEMAND, P. 1992 Lattice BGK for the Navier–Stokes equations. *Europhys. Lett.* **17**, 479–484.

RADL, S. & SUNDARESAN, S. 2014 A drag model for filtered Euler–Lagrange simulations of clustered gas–particle suspensions. *Chem. Engng Sci.* **117**, 416–425.

RICHARDSON, J. F. & ZAKI, W. N. 1954 Sedimentation and fluidisation. Part 1. *Trans. Inst. Chem. Engrs* **32**, 35–53.

SOMERS, J. A. 1993 Direct simulation of fluid flow with cellular automata and the lattice-Boltzmann equation. *Appl. Sci. Res.* **51** (1–2), 127–133.

SUNDARESAN, S. 2000 Modeling the hydrodynamics of multiphase flow reactors: current status and challenges. *AIChE J.* **46** (6), 1102–1105.

TENNETI, S., GARG, R. & SUBRAMANIAM, S. 2011 Drag law for monodisperse gas–solid systems using particle-resolved direct numerical simulation of flow past fixed assemblies of spheres. *Intl J. Multiphase Flow* **37**, 1072–1092.

WEN, C. Y. & YU, Y. H. 1966 Mechanics of fluidization. *Chem. Engng Prog.* **62**, 100–111.

WYLIE, J. J., KOCH, D. L. & LADD, A. J. C. 2003 Rheology of suspensions with high particle inertia and moderate fluid inertia. *J. Fluid Mech.* **480**, 95–118.

ZHOU, Q. & FAN, L. S. 2014 A second-order accurate immersed boundary-lattice Boltzmann method for particle-laden flows. *J. Comput. Phys.* **268**, 269–301.